Using excess ^{3}He to estimate Southern Ocean upwelling timescales

William J. Jenkins[1]

[1] Corresponding author; Woods Hole Oceanographic Institution, Woods Hole, MA 02543, U.S.A.
wjenkins@whoi.edu

Key Points

The Southern Ocean contains a distinct inventory of hydrothermally-sourced ^{3}He. Dividing this inventory by the global hydrothermal flux yields an estimate of an upwelling time-scale for deep waters in the Southern Ocean. The resulting estimate of approximately 60 years is relatively short compared to the estimated scavenging time for hydrothermally-sourced dissolved iron, suggesting that a significant fraction of the iron arrives at the sea surface to fuel new biological production.

Abstract

Using a recently compiled global marine dataset of dissolved helium isotopes and helium and neon concentrations, we make an estimate of the inventory of hydrothermal ^{3}He in the Southern Ocean to be $3.4 \pm 0.7 \times 10^{4}$ moles. Under the assumption that the bulk of the hydrothermally sourced ^{3}He is upwelled there, we use recent estimates of the global hydrothermal ^{3}He flux to determine an e-folding residence time of 62 ± 14 years, depending on assumptions of water mass and upwelling boundaries. Our estimate is comparable to values obtained from circulation models. The time-scale is at the lower end of the estimated scavenging life-time for dissolved iron (70 to 270 years), suggesting that a significant fraction of hydrothermally-sourced dissolved iron in the deep Pacific may reach the surface ocean to influence new primary production.

Plain Language Summary

Seafloor hydrothermal systems inject significant amounts of dissolved iron, but it remains unknown what fraction of that trace element survives *in situ* chemical scavenging to upwell in the Southern Ocean to arrive at the sea surface. Since iron a necessary trace-level nutrient for marine biological productivity, knowledge of the time it takes for deep water to rise to the surface is important. Along with dissolved iron, helium-3, a rare, inert isotope is also injected into the deep water. Since the global flux of this isotope has been independently determined by large-scale ocean models, we can estimate the upwelling time-scale by dividing it into the inventory of this isotope in the Southern Ocean.

Keywords & Index Terms

4808 Chemical Tracers

4207 Arctic and Antarctic oceanography

4845 Nutrients and nutrient cycling

4532 General circulation

4279 Upwelling and convergences

Other: Hydrothermal budgets; meridional overturning circulation; marine productivity; Southern Ocean upwelling; dissolved iron; micronutrients

1. Introduction

Recent observations of the large-scale distributions of dissolved iron and manganese in the abyssal South Pacific suggest that ocean ridge crest hydrothermal activity produces a significant flux of a dissolved phase for these metals that persists for many thousands of kilometers away from their injection sites (Fitzsimmons et al., 2014; Resing et al., 2015; Fitzsimmons et al., 2017). These large-scale horizontal plumes are also rich in hydrothermal ^{3}He (Resing et al., 2015; Jenkins et al., 2018). ^{3}He is an inert, unambiguous tracer of hydrothermal activity that has well-established global flux of 548 ± 52 mol a^{-1} (the weighted mean of estimates by Bianchi et al., 2010; Schlitzer, 2016; DeVries and Holzer, 2019). This allows the use of ^{3}He as a "flux gauge" to calculate the global hydrothermal fluxes for these trace metals by determining their concentrations relative to ^{3}He (Resing et al., 2015). The question of how this abyssal source of trace metals may eventually contribute to and influence global oceanic biological productivity pivots on what fraction of these metal fluxes survive deep water *in situ* scavenging processes (Bruland et al., 1994; Bergquist and Boyle, 2006; Fitzsimmons et al., 2014; Fitzsimmons et al., 2017). A first step in addressing this question involves establishing the time it takes for deep-water fluid parcels to upwell in the Southern Ocean.

Using a recently compiled global dataset of marine helium isotope observations (Jenkins et al., 2019a), we describe the basic characteristics of the distribution of this isotope in the Southern Ocean in relation to both its known sources and large scale circulation. We then compute the inventory of the excess (non-atmospheric) ^{3}He in the deep Southern Ocean and combine it with the estimated global hydrothermal ^{3}He flux to infer the time it takes for Pacific and Indian Ocean deep water fluid parcels to be upwelled in the Antarctic.

We begin by describing the distribution in terms of the most commonly used measure of non-atmospheric helium in the ocean, namely the dissolved helium isotope ratio anomaly relative to atmosphere, as defined by

$$\delta^3\mathrm{He} = \left(\frac{\left({}^3\mathrm{He}/{}^4\mathrm{He} \right)}{\left({}^3\mathrm{He}/{}^4\mathrm{He} \right)_{\mathrm{Air}}} - 1 \right) \times 100\% \ . \qquad (1)$$

The lighter isotope of helium is less soluble, so that water in equilibrium with the atmosphere has a negative ratio anomaly (between -1.6 and -1.8%, depending on temperature, see Benson and Krause, 1980), but this offset is predictable. The use of the helium isotope ratio anomaly is predicated on the fact that the hydrothermal helium introduced into the ocean is highly enriched in ^{3}He (Jenkins et al., 1978; Lupton and Craig, 1981), the rarer isotope of helium (Aldrich and Nier, 1948). The very earliest of these oceanic measurements were accurate to no better than 1 to 2%, but improved during and after the GEOSECS expeditions in the 1970s to the order of 0.1 to 0.3%, depending on laboratory or sampling and analysis methodology. We use a recently compiled global oceanic data-set of helium isotope and dissolved helium and neon concentration measurements retrieved from a variety of sources (Jenkins et al., 2019a) and is publically available at https://www.nodc.noaa.gov/ocads/data/0176626.xml . This dataset presently contains approximately 63,000 δ^3He, 57,000 dissolved helium concentration, and 34,000 dissolved neon concentration measurements. Although some of these measurements were made by the author, the bulk were made by other investigators, who are identified in the

database along with other metadata including quality control flags (Jenkins et al., 2019a). We initially describe only the δ^3He distribution from the perspective of the Southern Ocean, while the concentration data will become necessary for subsequent isotopic flux calculations later in this discussion.

2. The distribution of δ^3He in the Southern Ocean

Figure 1 is a map of δ^3He interpolated onto the 28.0 kg m^{-3} neutral density anomaly (computed according to Jackett and McDougall, 1997) surface. This level corresponds approximately to the core of the large ^{3}He plume observed to emanate from the East Pacific Rise at 15°S (Lupton and Craig, 1981; Jenkins et al., 2018). It appears to track the major trajectory of the ^{3}He-laden Pacific Deep Water (PDW) as it moves southward along the eastern boundary of the South Pacific and ultimately around the southern tip of South America (e.g., Well et al., 2003). By far the dominant feature of the global distribution on this horizon is the contrast between very high values (red trending to pink and white) in the Pacific and the relatively ^{3}He-impoverished waters (aqua to blue) of the Atlantic sector, with the Indian Ocean being intermediate (green to yellow). This contrast arises in large part from the direction of the planetary-scale meridional overturning circulation (the MOC, e.g., Kuhlbrodt et al., 2007). Newly ventilated waters move southward from the subarctic North Atlantic to join the Antarctic Circumpolar Current after it passes through the Drake Passage. From there, some of the Antarctic Circumpolar Deep Water (ACDW) mixture “peels off” to enter the abyssal Indian and then Pacific Oceans along their respective western boundaries. Within those basins, generalized upwelling feeds a returning mid-depth flow toward the Southern Ocean, where it ultimately upwells to the surface (Lumpkin and Speer, 2007; Talley, 2013) or forms intermediate waters. On these travels, the water accumulates hydrothermal ^{3}He (along with hydrothermal iron and manganese) from seafloor injection sites as it ages. The global contrast is accentuated by differences in mid-ocean ridge spreading rates between the Pacific and the other basins – the fastest spreading ridges tend to occur in the Pacific Ocean sector while the Atlantic and Indian oceans typically have slow spreading ridges. The flux of a primitive volatile like ^{3}He should be related to sea-floor spreading rates. Thus, the deep water in the Indian Ocean appears intermediate in δ^3He both because of its slower spreading ridges and its place in the MOC path.

The southward propagation of Pacific deep water (PDW) ^{3}He appears most pronounced in the southeast Pacific basin near the southern tip of South America. On the opposite side, between New Zealand and Australia, there is a northward bowing of δ^3He isopleths associated with the incursion of less δ^3He-enriched circumpolar waters into the Pacific (Stommel and Aarons, 1960; Warren, 1971). There is also evidence a similar feature in the southwest Indian Ocean, particularly around Madagascar expected from the deep western boundary current observed there (Warren, 1974). The Southern Ocean/Antarctic Circumpolar Current (ACC) regime appears as a pale blue band encircling the Antarctic continent, seemingly pushed northward by ^{3}He-impoverished (here depicted as darker blue) waters emanating from the Antarctic continent. This is especially evident in the Weddell Sea and to a lesser extent west of the Ross Sea and the Antarctic continental slope in between.

The three white lines in Fig.1 that extend radially from the coast of Antarctica around 30°E, 145°E, and 60°W mark hydrographic sections at three points along the Circumpolar Current, are shown in Fig 2. Note the color map used for these sections differs from that used in Figure 1 to match the observed range of values in those sections, and to make the vertical and horizontal

structure observed in the sections more visible. For comparison purposes, the white dashed line contour marks the δ^3He = 9% contour in each section. The black contour lines indicate neutral density anomaly levels (contour interval is 0.10 kg m^{-3}).

2.1 Antarctic to South Africa

There appear to be three subsurface δ^3He maxima associated with the ACCW in this sector of the Southern Ocean (Fig. 2a). The dominant feature, characterized by δ^3He values exceeding 9% (the white dashed contour line in all three sections), closely follows the 28.0 kg m^{-3} neutral surface and shoals from a maximum depth of ~2200 m at about 45°S to ~500 m at about 60°S. This maximum is clearly linked to the eastward Pacific Deep Water tongue in the Drake Passage that pivots around the tip of South America (Fig. 2c). The northern extent of this tongue in this section (around 54 – 55°S) is characterized by a significant northward decrease in nutrients along its isoneutral surface, marking a boundary between ACDW waters to the south and North Atlantic Deep Waters (NADW). To the north of this front is a weaker, less dense maximum centered on about 27.85 kg m^{-3} that extends to the South African coast. This corresponds to a silicate maximum that has been observed to extend throughout the South Atlantic (e.g., see Fig. 4 of Jenkins and Clarke, 1976) and appears in a much-diluted form in the subtropical North Atlantic. The deepest δ^3He maximum lies on a somewhat deeper neutral density anomaly horizon (28.2 kg m^{-3}) and extends further northward to around 43°S. As there appears to be no clear link with other hydrographic properties, it remains unclear whether this feature represents a unique water mass or is just an artifact of mixing between eastward flowing ACDW and northward moving Antarctic Bottom Water (AABW). Indeed, there is an appearance of this tongue spilling over the bottom topography. The ACDW complex is underlain by lower δ^3He AABW, with values around 5 – 6% in the south (between 51°S and the base of the Antarctic continental slope). To the north, a broad δ^3He minimum appears centered on 28.1 kg m^{-3}, the signature of lower nutrient, higher salinity NADW being entrained into the eastward flowing ACDW, perhaps to partly turn northward into the western Indian Ocean.

2.2 Antarctic to Australia

The mid-depth ACDW maximum in δ^3He extends over most of this section (Fig. 2b) and appears on a slightly denser neutral surface than the South African section, ranging from 28.05 kg m^{-3} in the south to 28.1 kg m^{-3} north of the Southeast Indian Ridge (SEIR). It approximately corresponds to a mid-depth salinity maximum as well as deep nitrate and phosphate secondary minima, although is somewhat shallower that these features south of 62°S and on average about 300 m deeper to the north. The pinching of the 9% δ^3He contour around 56°S corresponds to the minimum in eastward velocity south of the high velocity core of the ACC (Yaremchuck et al., 2001), and is suggestive of a layered structure (two maxima at 1300 and 2300 m, separated by a minimum in between). This appears to correspond to the northward deflection of transport streamlines as the ACC crosses the SEIR (Rintoul and Sokolov, 2001; Mccartney and Donohue, 2007) and may reflect a meridional interleaving of the mid-depth water masses associated with the crossing of rough topography. The mid-depth δ^3He maximum is more intense, approaching 14%, to the north of the Southeast Indian Ridge. It appears to highlight a deep anticyclonic recirculation exceeding 2 x 10^7 m^3 s^{-1} identified by others (Rintoul and Bullister, 1999; Rintoul and Sokolov, 2001; Yaremchuck et al., 2001; Mccartney and Donohue, 2007) with the southern part of the feature eastbound along the northern flank of the SEIR and the northern part westbound into the South Australia and Perth Basins. Examination of other WOCE helium/hydrographic sections to the west (I9S at ~120°E, I8S at ~85—95°E, and

I7S at ~60°E) within the context of the circulation scheme described by McCartney and Donohue (2007), reveals that the feature first appears at 90°E. Based on this, we conclude that the ^{3}He was acquired as the ACC passed through the Kerguelen-St. Paul Island Passage.

A distinct δ^3He maximum appears intermediated depths (1300 – 1700 m) in the northernmost station (supported by several data points). Values here approach 13.6%, higher than anywhere else in this section at this neutral density anomaly (27.7 kg m^{-3}). This must arise from the southwestward intrusion of waters from the Tasman Sea, indicative of a deeper penetration Tasman limb of the southern hemispheric oceanic super-gyre, which is more polar-intensified on AAIW strata (Ridgway and Dunn, 2007), but suggesting that this "Tasman leakage" extends deeper than previously recognized. Thus, some Pacific-derived volcanic helium is leaking into the Indian Ocean at these depths.

2.3 Antarctic to South America (Drake Passage)

The Drake Passage (Fig. 2c) represents the narrowest choke point for the ACC, where the current is forced to flow between the southern tip of South America and the northward extending West Antarctic Peninsula. At the southern side there is a residual δ^3He maximum centered on the 28.1 kg m^{-3} surface, but extending from 28.0 to 28.2 kg m^{-3}. The dominant feature of this section is the intense maximum along 28.0 kg m^{-3} in the north, a signature of ^{3}He-rich, deep Pacific waters leaking around the southern tip of South America (Well et al., 2003) into the eastward flowing ACC. Examination of three WOCE/CLIVAR meridional sections (P16S at ~150°W, P18S at ~105°W, and P19S at ~88°W) reveals a progressive southward extension of a broad, mid-depth δ^3He maximum spanning a range of neutral surfaces from 27.8 to 28.1 kg m^{-3}, that culminates in the "leakage" around the southwest Chilean coast into the Passage. Within the Drake Passage, the anomaly appears to extend to the bottom with waters slightly greater than 28.2 kg m^{-3}. This is likely a result of intense vertical mixing associated with passage through the choke point. Interestingly, we observe a shallower maximum at about 1500 m depth (27.8 kg m^{-3}) that occurs in only one station and was not observed by Well *et al.* (2003), which may indicate a spurious data point or a genuine feature that was missed due to station spacing. Above the 27.8 and below the 28.2 kg m^{-3} isoneutral surfaces the δ^3He and density contours appear to track within errors. South of the ACC one finds relatively low δ^3He water near the bottom with neutral density anomalies greater than 28.3 kg m^{-3}, which are associated with Antarctic Bottom Water originating from the Weddell Sea.

2.4 The general distribution

The overall picture is one of the Antarctic Circumpolar deep water (ACDW) having a δ^3He of ~10% that is intermediate between the hydrothermally enriched deep Pacific (~30%) and the relatively ^{3}He-poor ventilated end-members from the North Atlantic and Antarctic slope and embayments. The deep Indian Ocean appears slightly elevated (δ^3He~15%) compared to the ACDW. A simple mass transport calculation gives a rather similar ^{3}He transport across these three sections of the order of ~1000 mol a^{-1} (Jenkins et al., 2007), which is about twice the global hydrothermal ^{3}He flux (Bianchi et al., 2010; Schlitzer, 2016; DeVries and Holzer, 2019). In a sense, the ACDW is a "geochemical flywheel" that holds a hydrothermal ^{3}He inventory that passes through the Southern Ocean as it transits from the many seafloor injection points to its gradual and convoluted rise toward the ocean surface and its ultimate release to the atmosphere. Determining the magnitude of this inventory, and scaling it against the known flux, should yield a crude estimate of the upward transit time scale.

3. Determining the Southern Ocean volcanic ^{3}He inventories

In order to compute the Southern Ocean volcanic ^{3}He inventories, we must

- compute the molar concentration of non-atmospheric ^{3}He from the available data,
- define the vertical range over which to integrate those concentrations to obtain water column inventories,
- adopt an appropriate means of laterally interpolating/extrapolating the inventories onto a regular grid to minimize regional sampling biases, and
- define the appropriate geographic range over which to integrate the data.

In the following subsections we describe these steps

3.1 Computing the hydrothermal ^{3}He contribution

Following arguments developed earlier (Jenkins et al., 2018) we express the concentration of hydrothermal ("XS") ^{3}He in molar units using a semi-empirical relationship expressed by

$$C_{XS}\left(^3\mathrm{He}\right) = R_A\left[\left(1+\delta^3\mathrm{He}/100\right)C_M\left(^4\mathrm{He}\right) - \alpha_E C_S\left(^4\mathrm{He}\right) - 0.22\left(C_M\left(\mathrm{Ne}\right) - C_S\left(\mathrm{Ne}\right)\right)\right] \quad (2)$$

where the subscripts *S* and *M* signify solubility equilibrium and measured concentrations respectively, R_A is the atmospheric helium (^{3}He/^{4}He) isotope ratio (Clarke et al., 1976), and α_E is the helium solubility equilibrium isotope effect (Benson and Krause, 1980). The last term in the equation, involving neon concentrations, is an empirical correction for air injection by bubble dissolution near the sea surface, and is generally a small but significant term. The solubility concentrations are temperature and salinity dependent (Jenkins et al., 2019b) and are further corrected for a slight depth-dependent enhancement (~0.2 and ~0.3% for He and Ne respectively) that arises from diapycnal mixing effects (see Jenkins et al., 2018).

3.2 Calculating water column inventories

While the bulk of the global deep water upwelling occurs within the Southern Ocean (Marshall and Speer, 2012), some fraction of the hydrothermal helium entering the Southern Ocean must mix downward into the bottom waters to be swept northward into other basins. Since the bottom waters are generally impoverished in ^{3}He, it is logical to draw the inventory boundary between the two water masses. It can be argued that the lower limit of the Circumpolar Deep Waters inventory is essentially the boundary between the ^{3}He-enriched returning deep waters and those bottom water components that are formed around Antarctic and ultimately flow northward into the interiors of the subtropical ocean basins. The choice of the neutral density of that surface has a significant effect on the computed inventory, and could range between 28.11 (Orsi et al., 2002) and 28.18 kg m^{-3} (Orsi et al., 1999) to as deep as 28.26 (Garabato et al., 2002) to 28.27 kg m^{-3} (Jullion et al., 2014). Inasmuch as the volume, and hence our estimate of the total ^{3}He inventory depends on this parameter, we choose an intermediate value similar to Speer *et al.* (2000) of 28.20 kg m^{-3} and accept an intrinsic uncertainty in the resultant inventory as the range of values obtained between the two extremes (28.15 and 28.25 kg m^{-3}). The 28.20 kg m^{-3} contour seen in the three "choke point" sections shown in Fig. 2 delineates the downward penetration of the bulk of the hydrothermal ^{3}He mass, exemplified by the δ^3He = 9% contour. Winckler *et al* (2010) reported a potential hydrothermal source in the Pacific sector of the Southern Ocean centered at the 28.2 kg m^{-3} neutral surface, which may contribute to the deeper tongue at the northern end of the Antarctic-South Africa section. Our choice may neglect that contribution, but it is likely a

relatively small perturbation compared to the major portion of the hydrothermal ^{3}He features entering the Southern Ocean above or near the 28.1 kg m^{-3} horizon.

The dataset (Jenkins et al., 2019a) was filtered such that only data with corresponding neon measurements that exhibited saturation anomalies between -5% and +20% to avoid obviously contaminated or compromised measurements. A station's hydrothermal ^{3}He inventory was computed using a tensioned smoothing spline (to avoid spurious peaks) and only accepted if there were at least four discrete measurements made within the density range of interest (between the surface and 28.20 kg m^{-3}). Profiles were visually scanned to ensure anomalous results were avoided. In all, inventories at 109 locations were computed within the geographic range of interest (see black dots in Figure 4 and the next section).

3.3 Laterally summing water column inventories

The individual station inventories were gridded as a function of latitude and longitude onto a 1° resolution mesh using a GMT minimum curvature gridding routine ("surface", using a tension of 0.25, Smith and Wessel, 1990; Wessel and Smith, 2008). The objective was to minimize the effects of sampling bias by smoothly extrapolating into areas of no/low coverage, avoiding generation of spurious extrema, and generally producing a reasonable looking distribution based on knowledge of other property distributions. Although other gridding methods will produce different results, variations in inventory estimates driven by uncertainties associated with the bounds of integration (both vertical and horizontal) make such refinements moot.

In order to establish the appropriate ^{3}He inventory, we must define the geographical bounds of the CDW ^{3}He distribution in the deep Southern Ocean, and more specifically the northern extent of the region where upwelling may occur. Consideration of the distribution of the large lateral volcanic ^{3}He plumes in the Pacific, it is evident that where the 28.00 km m^{-3} neutral density surface begins to rise up toward the surface in its southward journey would be the appropriate boundary. Figure 3a depicts the trends in the depth of the 28.00 km m^{-3} neutral density surface as a function of latitude for each ocean, as extracted from the WOA13 (Locarnini et al., 2013; Zweng et al., 2013). We select the 2200 m as the horizon where this upwelling nominally commences. Figure 3b is a map of the 2200 m depth contour for the 28.00 kg m^{-3} surface (note we use the southernmost circum-Antarctic contour is the CDW northern boundary). Figure 4 is a map of the resultant water column ^{3}He inventories in nmol m^{-2} above 28.2 kg m^{-3} horizon. The black dots signify the location of the stations used to construct the map. At each longitude, the gridded inventory distribution is integrated southward from this contour using area (latitude) weighting until either the 28.20 kg m^{-3} horizon outcrops, or the 150 m isobath is encountered.

Using the above method, we calculate inventory of ^{3}He in the Southern Ocean to be 3.40 x 10^4 mol. If we extend the integration volume to the 28.25 kg m^{-3} horizon, the value increases 4.12 x 10^4 mol. Conversely, if we reduce the volume to the 28.15 kg m^{-3} surface, the inventory decreases to 2.65 x 10^4 mol. Thus, we adopt an inventory estimate of 3.4 $\pm$ 0.7 x 10^4 mol.

4. Discussion

Dividing this inventory by our best estimate of the global hydrothermal ^{3}He flux of 548 $\pm$ 52 mol a^{-1} (we use a weighted mean of the estimates by Bianchi et al., 2010; Schlitzer, 2016; DeVries and Holzer, 2019), we obtain an e-folding upwelling timescale of 62 $\pm$ 14 years. The uncertainty is derived from propagation of errors in the inventory and flux estimates. The corresponding

half-life for upwelling would be 43 ± 10 years. By comparison, using a combination of hydrographic analysis and particle trajectories from high resolution Southern Ocean model simulations, Tamsitt *et al.* (2017) estimate an upwelling half-time of 60-90 years, which appears consistent with our analysis. Although it is tempting to interpret these time scales within the framework of transit time distributions, recent work has indicated that simple spectral functions such as the inverse Gaussian do not apply well to Southern Ocean upwelling (Trossman et al., 2014). Drake *et al.* (2018) use a hierarchy of models exhibiting Southern Ocean Lagrangian upwelling timescales that decline from 87 to 17 years with increasing resolution. Our estimate, based on a simple box-model flushing time is at the higher end of that range.

These determinations of the Southern Ocean deep water upwelling timescale falls at the lower end of the range of estimated dissolved iron scavenging timescales for the abyssal ocean (70 to 270 years, see Bruland et al., 1994; Berquist and Boyle, 2006). This suggests that a significant fraction of the dissolved iron (dFe) released into the deep waters from hydrothermal activity (Boyle and Jenkins, 2008; Resing et al., 2015; Fitzsimmons et al., 2017) may survive to act as a controlling micronutrient for new production in the Southern Ocean. However, knowledge of precisely how much of this hydrothermal dissolved iron does reach the surface will depend on a refinement of our understanding of both the pathways, timescales, and dissolved iron scavenging rates. This also suggests that the distribution of ^{3}He/dFe ratios in the Southern Ocean may further inform us of those processes affecting that metal's concentrations in the ocean.

Acknowledgements

The author is grateful to all those dedicated analysts and seagoing support groups that have toiled to create a global dataset of marine helium isotope measurements. I also thank Bob Anderson for inspiring this endeavor. This work was funded under the auspices of the U.S. National Science Foundation's grant OCE-1756138. All of the data used in this publication are openly available from the U.S. National Oceanic and Atmospheric Administration's National Centers for Environmental Information at https://www.nodc.noaa.gov/ocads/data/0176626.xml a the dataset's DOI is 10.25921/c1sn-9631.

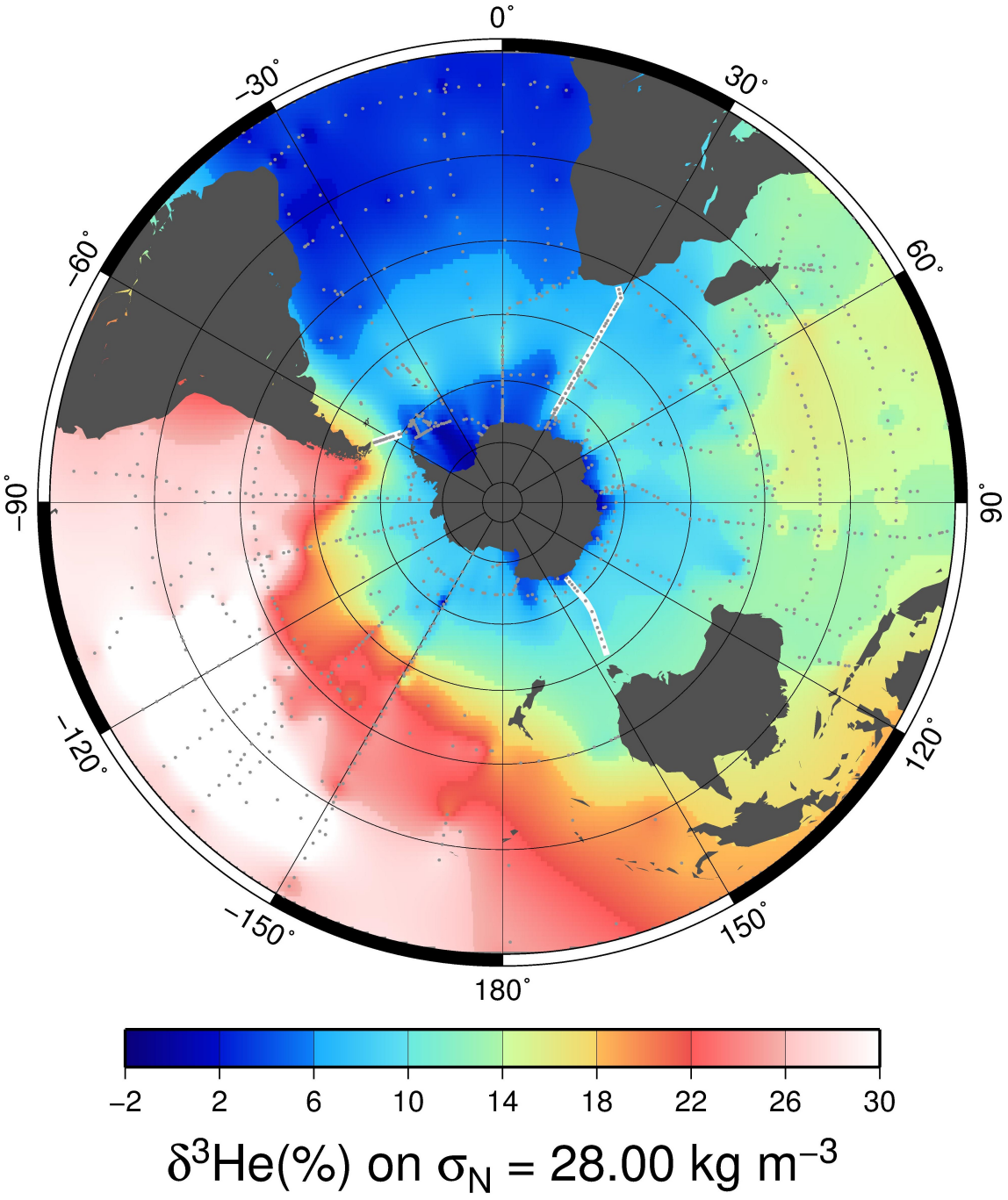

Figure 1: The distribution of δ^3He (in %) on a key neutral surface (σ_N = 28.0 kg m^{-3}). This density horizon corresponds to the core of the South Pacific hydrothermal ^{3}He plume (Jenkins et al., 2018). The main features include the dominance of the Pacific Deep Water, a weaker but significant contribution from the Indian Ocean, and the ^{3}He-impoverished North Atlantic Deep Water in the Atlantic sector. Note also the low ^{3}He waters surrounding the Antarctic continent. The gray dots denote station locations. The white lines (partially obscured by station marks) correspond to the sections shown in the next figure.

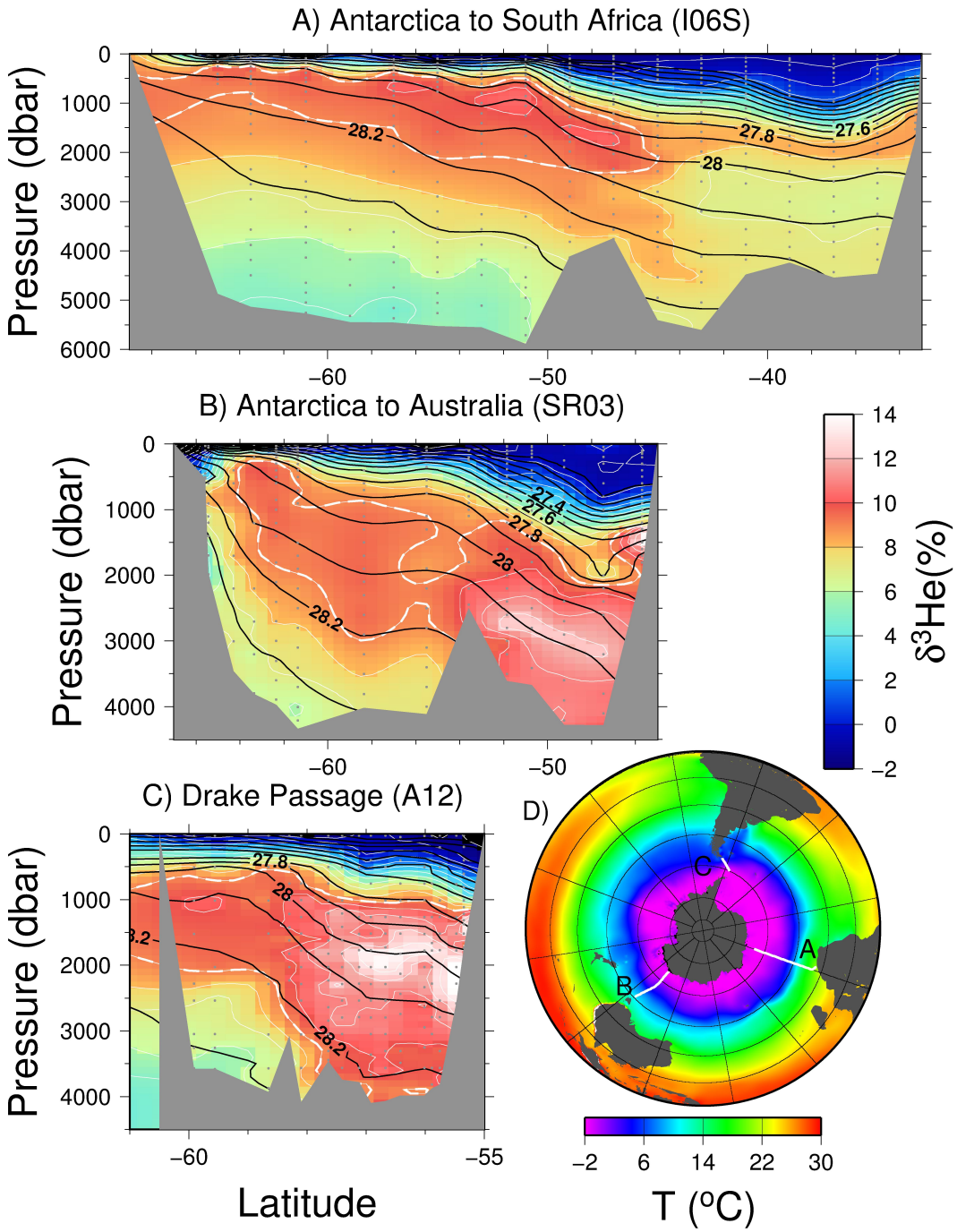

Figure 2: The depth distributions of δ^3He for the three sections denoted by the solid white lines in Figure 1. Note the different δ^3He color scale. Gray dots signify sample locations. The dashed white line corresponds to δ^3He = 9%. The black contours are neutral density with an interval of 0.1 kg/m^3. Antarctica is on the left for all three sections taken (A) from South Africa to Antarctic, (B) from Australia to Antarctica, and (C) across the Drake Passage. The map (D) shows the section locations overlaying Austral winter sea surface temperature obtained from the World Ocean Atlas 2013 (Locarnini et al., 2013) .

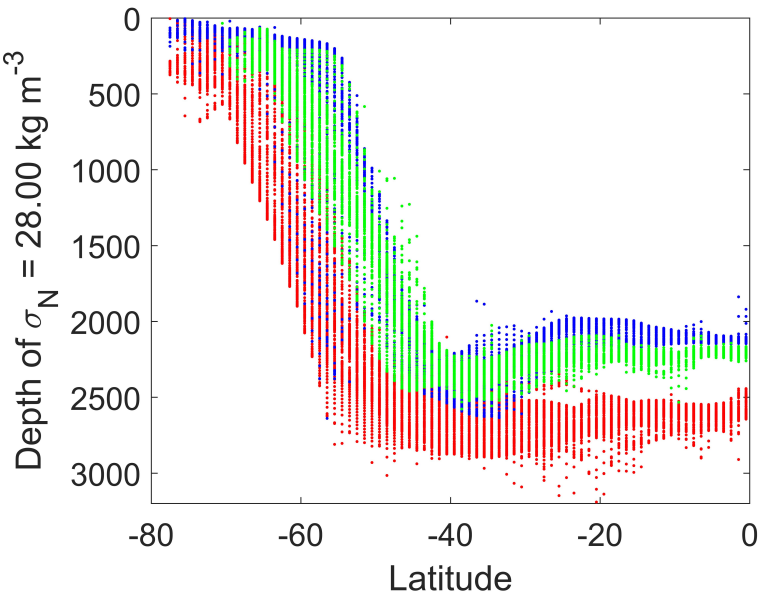

Fig 3a: The depth of the 28.00 kg m^{-3} neutral density anomaly surface as a function of latitude from the World Ocean 2013 Atlas. The red, green, and blue points correspond to the Pacific, Indian, and Atlantic Ocean sectors respectively.

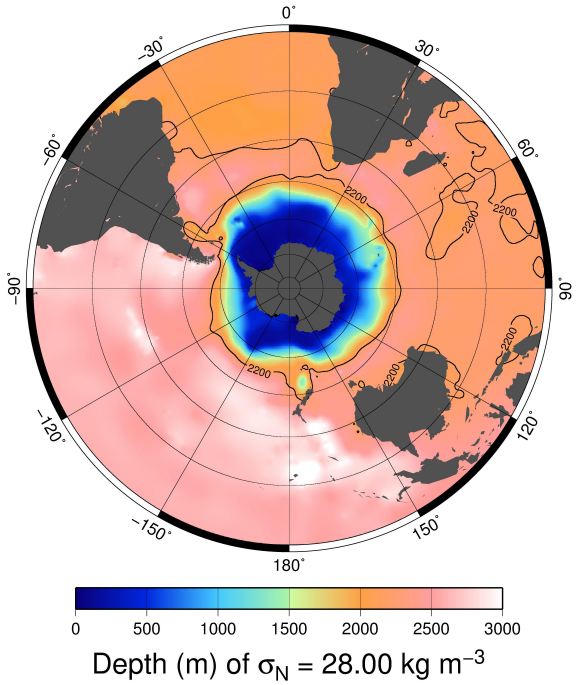

Fig 3b: A map of the 28.00 kg m^{-3} neutral density anomaly surface 2200 m depth contour. The southernmost contour is used to define the northern boundary of the integration volume.

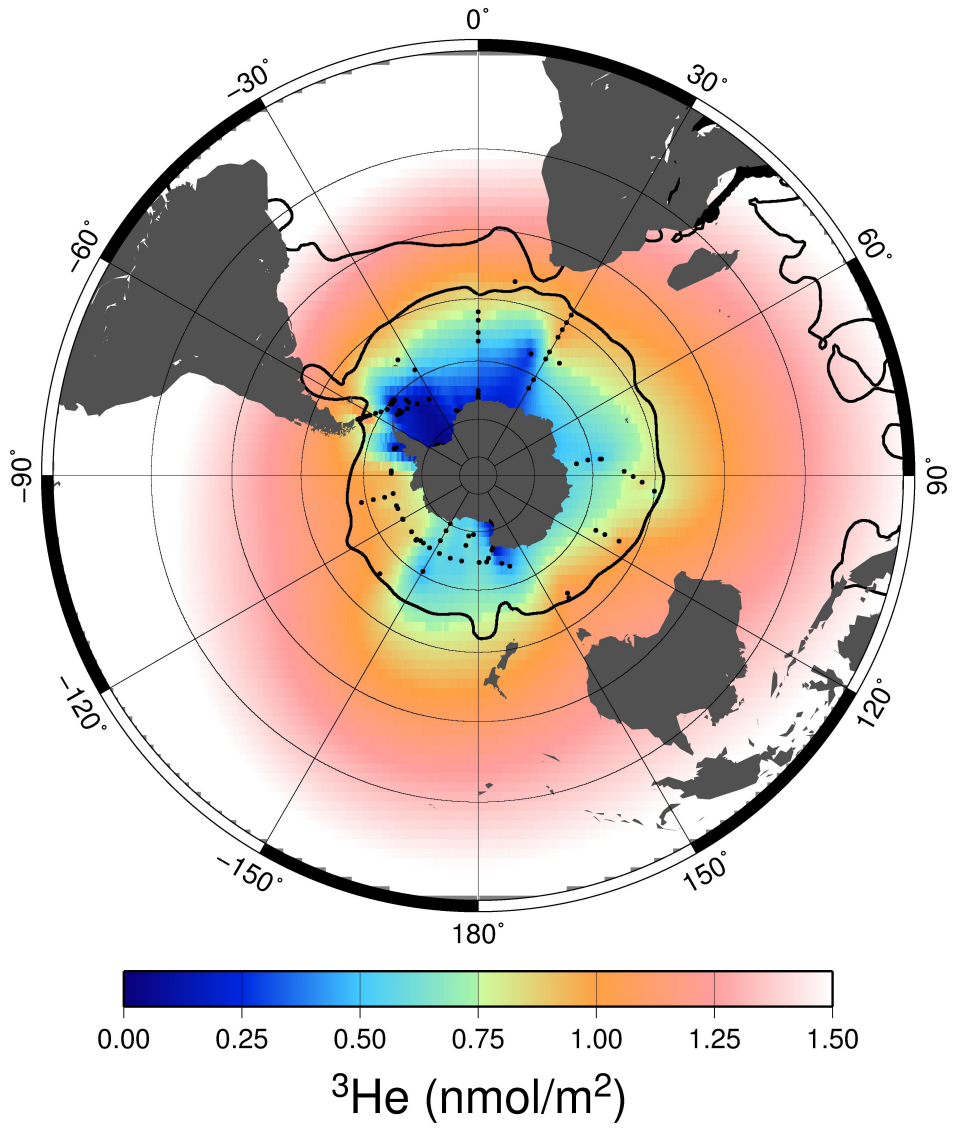

Fig4: A map of the computed ^{3}He water column inventories in nmol m^{-2} above the 28.20 kg m^{-3} horizon (or seafloor).

References

Aldrich, L.T. and Nier, A.O., 1948. The occurrence of ^{3}He in natural sources of helium. Physical Review, 74(11): 1590-1594.

Benson, B.B. and Krause, D., Jr., 1980. Isotopic fractionation of helium during solution: a probe for the liquid state. Journal of Solution Chemistry, 9: 895-909.

Bergquist, B.A. and Boyle, E.A., 2006. Dissolved iron in the tropical and subtropical North Atlantic. Global Biogeochemical Cycles, 20(GB1015): doi:10.1029/2005GB002505.

Berquist, B.A. and Boyle, E.A., 2006. Dissolved iron in the tropical and subtropical Atlantic Ocean. Global Biogeochemical Cycles, 20: GB1015.

Bianchi, D., Sarmiento, J.L., Gnanadesikan, A., Key, R.M., Schlosser, P. and Newton, R., 2010. Low helium flux from the mantle inferred from simulations of oceanic helium isotope data. Earth and Planetary Science Letters, 297: 379-386.

Boyle, E. and Jenkins, W.J., 2008. Hydrothermal iron in the deep western South Pacific. Geochimica et Cosmochimica Acta, 72(12S): A107.

Bruland, K.W., Orians, K.J. and Cowen, J.P., 1994. Reactive metals in the stratified central North Pacific. Geochimica et Cosmochimica Acta, 58(15): 3171-3182.

Clarke, W.B., Jenkins, W.J. and Top, Z., 1976. Determination of tritium by spectrometric measurement of ^{3}He. International Journal of Applied Radiation and Isotopes, 27: 515-525.

DeVries, T. and Holzer, M., 2019. Radiocarbon and helium isotope constraints on deep-ocean ventilation and mantle-^{3}He sources. Journal of Geophysical Research: Oceans, 124(5): 3036-3057.

Drake, H.F., Morrison, A.K., Griffies, S.M., Sarmiento, J.L., Weijer, W. and Gray, A.R., 2018. Lagrangian timescales of Southern Ocean upwelling in a hierearhy of model resolutions. Geophysical Research Letters, 45: 891-898.

Fitzsimmons, J.N., Boyle, E.A. and Jenkins, W.J., 2014. Distal transport of dissolved hydrothermal iron in the deep South Pacific Ocean. Proc Natl Acad Sci U S A, 111(47): 16654-16661.

Fitzsimmons, J.N., John, S.G., Marsay, C.M., Hoffman, C., Nicholas, S., Toner, B.M., German, C.R. and Sherrell, R.M., 2017. Iron persistence in a distal hydrothermal plume supported by dissolved-particulate exchange. Nature Geoscience, 10: 195-201.

Garabato, A.C.N., McDonagh, E.L., Stevens, D.P., Heywood, K.J. and Sanders, R.J., 2002. On the export of Antarctic Bottom Water from the Weddell Sea. Deep-Sea Research II, 49: 4715-4742.

Jackett, D.R. and McDougall, T.J., 1997. A neutral density variable for the world's oceans. Journal of Physical Oceanography, 27(2): 237-263.

Jenkins, W.J. and Clarke, W.B., 1976. The distribution of ^{3}He in the western Atlantic Ocean. Deep-Sea Research, 23: 481-494.

Jenkins, W.J., Doney, S.C., Fendrock, M., Fine, R.A., Gamo, T., Jean-Baptiste, P., Key, R., Klein, B., Lupton, J.E., Newton, R., Rhein, M., Roether, W., Sano, Y., Schlitzer, R., Schlosser, P. and Swift, J.H., 2019a. A comprehensive global oceanic dataset of helium isotope and tritium measurements. Earth System Science Data, 11: 441-454.

Jenkins, W.J., Edmond, J.M. and Corliss, J.B., 1978. Excess ^{3}He and ^{4}He in Galapagos submarine hydrothermal waters. Nature, 272: 156-158.

Jenkins, W.J., Lott, D.E., III and Cahill, K.L., 2019b. A Determination of Atmospheric Helium, Neon, Argon, Krypton, and Xenon Solubility Concentrations in Water and Seawater. Marine Chemistry, 211(1): 94-107.

Jenkins, W.J., Lott, D.E., III, German, C.R., Cahill, K.L., Goudreau, J. and Longworth, B.E., 2018. The deep distributions of helium isotopes, radiocarbon, and noble gases along the U.S. GEOTRACES East Pacific zonal transect (GP16). Marine Chemistry, 201(1): 167-182.

Jenkins, W.J., Naveira Garabato, A.C., Schlosser, P., Lott, D.E.I. and Newton, R., 2007. Oceanic volcanic ^{3}He: where is it going? EOS Transactions AGU, 2007 Fall Meeting Abstracts.

Jullion, L., Garabato, A.C.N., Bacon, S., Meredith, M.P., Brown, P.J., Torres-Valdes, S., Speer, K.G., Holland, P.R., Dong, J., Bakker, D., Hoppema, M., Loose, B., Venables, H.J., Jenkins, W.J., Messias, M.J. and Fahrbach, E., 2014. The contribution of the Weddell Gyre to the lower limb of the Global Overturning Circulation. Journal of Geophysical Research-Oceans, 119(6): 3357-3377.

Kuhlbrodt, T., Griesel, A., Montoya, M., Levemann, A., Hofmann, M. and Rahmstorf, S., 2007. On the driving processes of the Atlantic meridional overturning circulation. Reviews of Geophysics, 45(RG2001): doi:10.1029/2004RG000166.

Locarnini, R.A., Mishonov, A.V., Antonov, J.I., Boyer, T.P., Garcia, H.E., Baranova, O.K., Zweng, M.M., Paver, C.R., Reagan, J.R., Johnson, D.R., Hamilton, M. and Seidov, D., 2013. Temperature. In: S. Levitus and A.T. Mishonov (Editors), World Ocean Atlas 2013. NOAA, Silver Springs, MD, pp. 40.

Lumpkin, R. and Speer, K., 2007. Global ocean meridional overturning. Journal of Physical Oceanography, 37(10): 2550-2562.

Lupton, J.E. and Craig, H., 1981. A major helium-3 source at 15S on the East Pacific Rise. Science, 214(4516): 13-18.

Marshall, J. and Speer, K., 2012. Closure of the meridional overturning circulation through Southern Ocean upwelling. Nature Geoscience, 5(3): 171-180.

Mccartney, M.S. and Donohue, K.A., 2007. A deep cyclonic gyre in the Australian-Antarctic Basin. Progress in Oceanography, 75: 675-750.

Orsi, A.H., Johnson, G.C. and Bullister, J.L., 1999. Circulation, mixing, and production of Antarctic Bottom Water. Progress in Oceanography, 43: 55-109.

Orsi, A.H., Smethie, W.M. and Bullister, J.L., 2002. On the total input of Antarctic waters to the deep ocean: a preliminary estimate based on chlorofuorocarbon measurements. Journal of Geophysical Research, 107(C8): 10.109/2001JC000976.

Resing, J.A., Sedwick, P.N., German, C.R., Jenkins, W.J., Moffett, J.W., Sohst, B.M. and Tagliabue, A., 2015. Basin-Scale transport of hydrothermal dissolved metals across the South Pacific Ocean. Nature, 523(9 July 2015): 203-206.

Ridgway, K.R. and Dunn, J.R., 2007. Observational evidence for a southern hemisphere oceanic supergyre. Geophysical Research Letters, 34(L13612): doi:10.1029/2007GL030392, 2007.

Rintoul, S. and Bullister, J.L., 1999. A late winter hydrographic section from Tasmania to Antarctica. Deep Sea Research Part I: Oceanographic Research Papers, 46: 1417-1454.

Rintoul, S.R. and Sokolov, S., 2001. Baroclinic transport variability of the Antarctic Circumpolar Current south of Australia (WOCE repeat section SR3). Journal of Geophysical Research, 106(C2): 2815-2832.

Schlitzer, R., 2016. Quantifying He fluxes from the mantle using multi-tracer data assimilation. Philosophical Transactions of the Royal Society of London Series a-Mathematical Physical and Engineering Sciences, 374(2081): DOI: 10.1098/rsta.2015.0288.

Smith, W.H.F. and Wessel, P., 1990. Gridding with continuous curvature splines in tension. Geophysics, 55(3): 293-305.

Speer, K.G., Rintoul, S.R. and Sloyan, B.M., 2000. The diabatic Deacon Cell. Journal of Physical Oceanography, 30(12): 3212-3222.

Stommel, H. and Aarons, A.B., 1960. On the abyssal circulation of the world ocean - II. An idealized model of the circulation pattern and amplitude in ocean basins. Deep-Sea Research, 6: 217-233.

Talley, L.D., 2013. Closure of the global overturning circulation through the Indian, Pacific, and Southern Oceans: Schematics and transports. Oceanography, 26(1): 80-97.

Tamsitt, V., Drake, H.F., Morrison, A.K., Talley, L., Dufour, C.O., Gray, A.R., Griffies, S.M., Mazloff, M.R., Sarmiento, J.L., Wang, J. and Weijer, W., 2017. Spiraling pathways of global deep waters to the surface of the Southern Ocean. Nature Communications, 8: DOI: 10.1038/s41467-017-00197-0.

Trossman, D.S., Thompson, L., Mecking, S., Warner, M.J., Bryan, F.O. and Peacock, S., 2014. Evaluation of oceanic transport parameters using transient tracers from observations and model output. Ocean Modelling, 74: 1-21.

Warren, B.A., 1971. Evidence for a deep western boundary current in the South Indian Ocean. Nature, 229(1): 18-19.

Warren, B.A., 1974. Deep flow in the Madagascar and Mascarine basins. Deep-Sea Research, 21: 1-21.

Well, R., Roether, W. and Stevens, D.P., 2003. An additional deep-water mass in Drake Passage as revealed by ^{3}He data. Deep-Sea Research I, 50(9): 1079-1098.

Wessel, P. and Smith, W.H.F., 2008. The Generic Mapping Tools Version 4.3.1 A Map-making Tutorial. School of Ocean and Earth Science and Technology, University of Hawaii at Manoa, Honolulu, pp. 25.

Winckler, G., Newton, R., Schlosser, P. and Crone, T.J., 2010. Mantle helium reveals Southern Ocean hydrothermal venting. Geophysical Research Letters, 37(L05601): doi:10.1029/2009GL042093.

Yaremchuck, M., Bindoff, N.L., Schroter, J., Nechaev, E. and Rintoul, S.R., 2001. On the zonal and meridional circulation and ocean transports between Tasmania and Antarctica. Journal of Geophysical Research, 106(C2): 2795-2814.

Zweng, M.M., ., Reagan, J.R., Antonov, J.I., Locarnini, R.A., Mishonov, A.V., Boyer, T.P., Garcia, H.E., Baranova, O.K., Johnson, D.R., Seidov, D. and Biddle, M.M., 2013. Salinity. In: S. Levitus and A.T. Mishonov (Editors), World Ocean Atlas 2013. NOAA Atlas NESDIS. NOAA, Silver Springs, MD, pp. 39.